RSC Advances

PAPER

View Article Online
View Journal | View Issue

Cite this: *RSC Adv.*, 2026, **16**, 12256

Enhanced electrochemical performance with Co-V-O bridges and dual active sites for water electrolysis applications

Kangkang Zhao,†[ac] Yongren Yu,†[b] Yixuan Jia,[a] Yunjie Ke,[a] Jian Wang,[a] Shiwei Song,[a] Yucai Li,[c] Fang Hu,[b] Depeng Zhao [c] and Lihua Miao *[ac]

Vanadium pentoxide (V_2O_5) exhibits broad application prospects in the field of battery cathode materials due to its layered structure and high theoretical specific capacity. However, its inherent low electrical conductivity and structural instability during cycling severely restrict its electrochemical performance. To overcome these bottlenecks, cobalt (Co)-doped V_2O_5 materials were successfully prepared *via* a hydrothermal synthesis method in this study. Characterization confirmed that Co ions were successfully incorporated into the V_2O_5 lattice, which effectively expanded the interlayer spacing and improved the electronic conductivity of the material. Electrochemical test results showed that compared with pure V_2O_5, the Co-V_2O_5 sample demonstrated excellent hydrogen evolution reaction and oxygen evolution reaction performances, with lower overpotentials and Tafel slopes. As a catalyst for driving water electrolysis, the sample exhibited a cell voltage of 1.38 V at 10 mA cm^{-2} and excellent long-cycle stability.

Received 7th January 2026
Accepted 26th February 2026

DOI: 10.1039/d6ra00151c

rsc.li/rsc-advances

1. Introduction

With the development of modern society, traditional fossil fuels can hardly meet long-term demands due to limited resources and environmental issues. Hydrogen energy has thus emerged as an ideal alternative energy source. Water splitting is an effective method for hydrogen production,[1–5] which involves the hydrogen evolution reaction and oxygen evolution reaction. In electrocatalysis, the performance of catalysts determines the efficiency and cost of devices.[6–8] Although noble metal catalysts exhibit high activity, their high price and insufficient stability prevent them from meeting the requirements of long-term operation. Therefore, developing electrocatalysts with low cost and excellent performance is a core research direction currently. These catalysts can reduce activation energy, accelerate reactions, improve energy conversion efficiency and economy, and lay the foundation for industrialization.[9–13]

Vanadium pentoxide (V_2O_5), as a transition metal oxide, has advantages such as wide availability, low cost, and easy synthesis. Its unique layered crystal structure is suitable for the intercalation and deintercalation of metal ions. However, it faces many challenges in practical applications: its inherent electrical conductivity is low, and poor kinetic performance during charge–discharge processes leads to rapid attenuation of battery capacity.[14–18] To overcome these limitations of the material, doping metal cations into vanadium pentoxide is a simple and effective method.[19–21] Liu and colleagues compared V_2O_5 doped with different cations (Fe, Co, Ni) and found that vanadium pentoxide doped with Co ions exhibited excellent electrochemical performance. In particular, the introduction of Co ions significantly enhanced the conversion kinetics of Localized interfacial polarization sites (LIPSs).[22] Zong and colleagues intercalated Zn^{2+} into V_2O_5, which expanded the lattice spacing, promoted ion diffusion kinetics, maintained the stability of the layered structure, and effectively improved cycle stability and cycle life.[23–26]

In this study, we prepared cobalt-doped V_2O_5 materials *via* a simple hydrothermal synthesis method. Compared with pure V_2O_5, the Co-V_2O_5 samples exhibited excellent HER and OER performances in different electrolyte environments, with lower overpotentials and Tafel slopes. As a catalyst for driving water electrolysis, the sample showed a cell voltage of 1.38 V at 10 mA cm^{-2} and excellent stability after 12 hours of cycling.

2. Experimental section

2.1 Preparation of Co-V_2O_5 nanomaterials

Before material synthesis, the nickel foam (2 × 3 cm^{-2}) required for the experiment needs to be pretreated to remove surface impurities and grease. The prepared nickel foam was

[a]School of Medical Information Engineering, Shenyang Medical College, Shenyang, Liaoning, 110034, P. R. China. E-mail: miaolihua@symc.edu.cn
[b]School of Materials Science and Engineering, Shenyang University of Technology, Shenyang 110870, P. R. China
[c]School of New Energy, Shenyang Institute of Engineering, CN 110136, Shenyang, Liaoning, P. R. China
† These authors contributed equally.

immersed in 1 M HCl and sonicated for 30 minutes, then repeatedly cleaned with deionized water and ethanol, followed by drying for later use.

The synthesis steps of Co-V_2O_5 samples were as follows: add 0.9 g of V_2O_5 powder, 1.89 g of oxalic acid, and 50 mL of water into a 100 mL beaker. Stir the mixture at a constant temperature of 80 °C until the powder is completely dissolved. After cooling to room temperature, add 30% H_2O_2 and continue stirring.Then add ethanol and x mg (x = 0.03, 0.06, 0.09) of $Co(NO_3)_2 \cdot 6H_2O$. Transfer the solution into a 100 mL autoclave and heat it at 170 °C for 8 hours. After natural cooling, take out the synthesized product, clean it, dry it, and then calcine it. Finally, grind the synthesized product and coat it on the prepared nickel foam. The corresponding samples are denoted as Co-V_2O_5-3%, Co-V_2O_5-6%, and Co-V_2O_5-9% respectively.

3. Results and discussion

3.1 Structural characterization of materials

The crystal structure of the target material is shown in the Fig. 1a. The figure presents the XRD patterns of pure V_2O_5 and V_2O_5 with different cobalt doping contents. The blue curve shows the diffraction peaks of pure-phase V_2O_5 powder, with no other impurity peaks observed. The diffraction peaks at 2θ values of 15.3°, 20.3°, 26°, 31°, and 32.3° correspond to the (200), (001), (110), (400), and (011) crystal planes of the V_2O_5 phase (JCPDS No. 41-1426), respectively. Compared with pure V_2O_5, the Co-doped V_2O_5 materials also exhibit the same diffraction peaks, and no impurity peaks (that are absent in pure V_2O_5) are detected. When comparing the (110) crystal plane near 26°, it can be observed that the introduction of Co causes a small-angle shift in the diffraction peak of the (110) crystal plane of V_2O_5. The potential reason may be that the incorporation of Co ions changes the lattice size of V_2O_5, confirming the successful doping of Co into V_2O_5.

Subsequently, the chemical valence states and elemental composition of the material surface were evaluated using X-ray photoelectron spectroscopy.[27] As shown in Fig. 1b, the V 2p spectrum reveals the change in V valence states caused by doping. In the V 2p spectrum, V^{5+} is located at binding energies of 517.2 eV and 524.3 eV, while the binding energies of V^{4+} are 516.2 eV and 523.4 eV, respectively. The change in vanadium ion valence states indicates that Co^{2+} is successfully doped into the lattice of V_2O_5. The O 1s spectrum is shown in Fig. 1c. As shown in the figure, a large number of oxygen vacancies appear at 531.5 eV, which indicates that Co ion doping can induce the generation of a large number of oxygen vacancies in V_2O_5. For Co-V_2O_5, the other two peaks at 530.5 eV and 532.5 eV are attributed to V–O bonds and crystal water in Co-V_2O_5, respectively. As shown in Fig. 1d, the Co 2p energy spectrum of Co-V_2O_5 exhibits characteristic peaks with binding energies of 780.6 eV and 797.3 eV, each followed by two satellite peaks. This confirms that Co is doped into Co-V_2O_5 in the form of Co^{2+}.

Scanning electron microscopy (SEM) is used for morphological characterization. The SEM images of V_2O_5 and Co-V_2O_5 catalysts are presented in Fig. 2a–b. Fig. 2a and b are low-magnification and high-magnification SEM images of pure

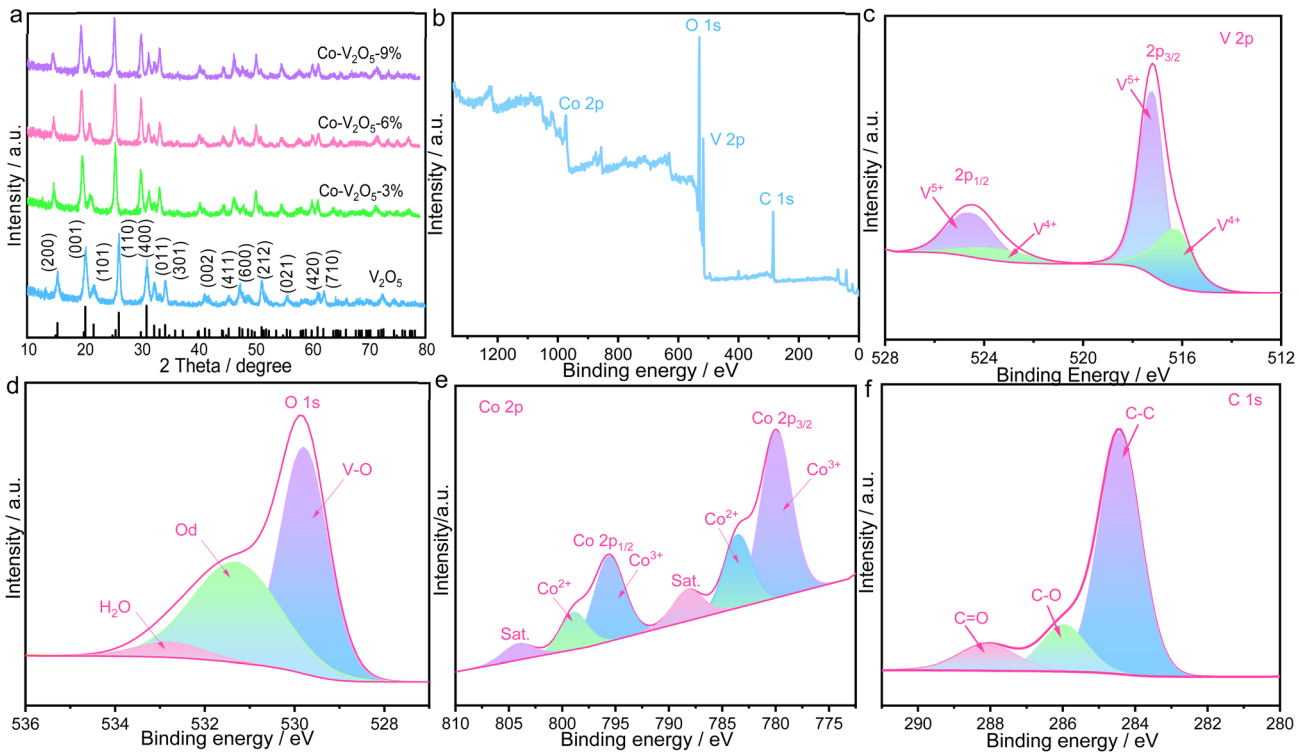

Fig. 1 Structural characterization of the prepared samples (a) XRD patterns of V_2O_5 and V_2O_5 with different Co doping contents. (b) Survey XPS spectrum (c) XPS spectrum of V 2p. (d) O 1s (e) Co 2p (f) C 1s.

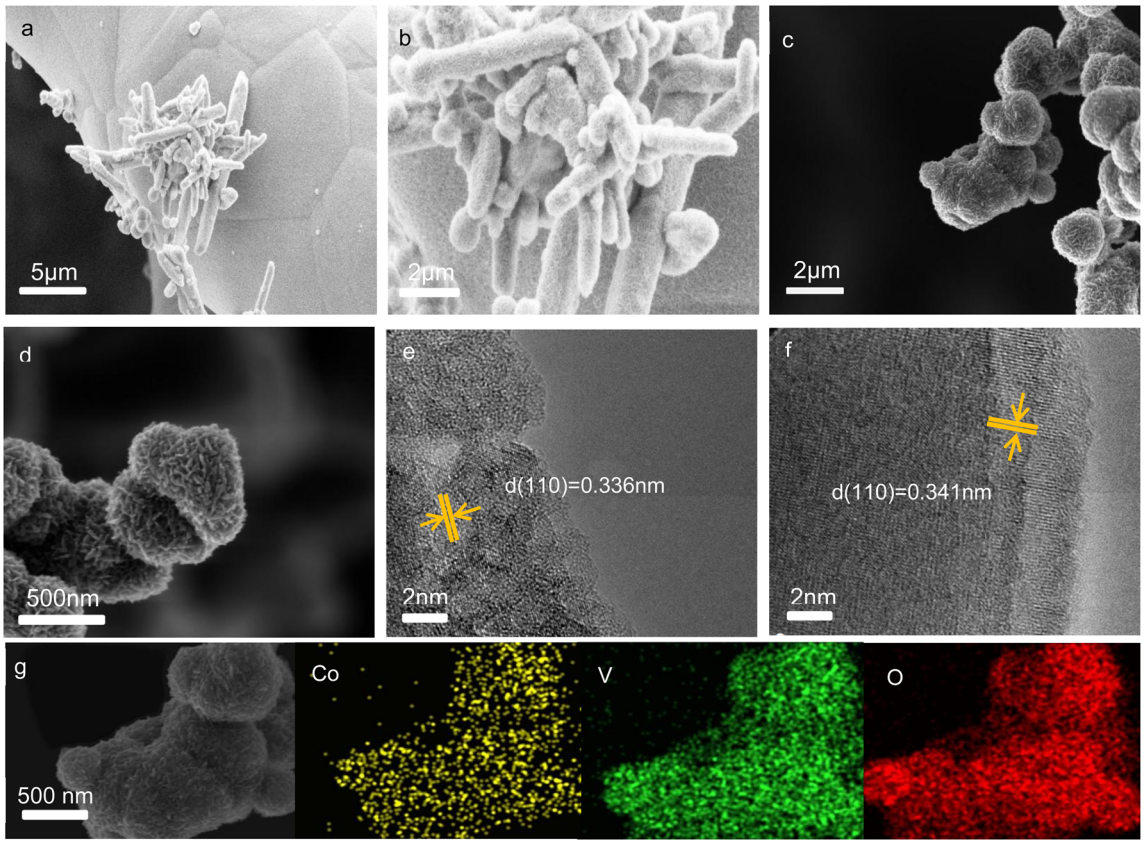

Fig. 2 Morphological and structural characterization of the prepared products (a) low-magnification SEM image of V_2O_5 (b) high-magnification SEM image of V_2O_5 (c) low-magnification SEM image of Co-V_2O_5 (d) high-magnification SEM image of Co-V_2O_5 (e) HRTEM image of the V_2O_5 sample (f) Co-V_2O_5 (g) elemental mapping image of the Co-V_2O_5 sample.

V_2O_5, respectively. From the low-magnification SEM image, it can be observed that pure V_2O_5 exhibits a nanorod shape and adheres to the smooth nickel foam skeleton, but it also shows a certain degree of agglomeration. Such massive accumulation of V_2O_5 nanorods may be caused by the aggregation of V_2O_5 crystal nuclei in the initial stage of the reaction, which results in insufficient exposure of active sites on the V_2O_5 nanorods. From the high-magnification SEM image, it can be seen that each nanorod is intertwined, with an average size of 5 μm and a relatively smooth surface.

The morphology of Co-V_2O_5 nanospheres after Co doping is shown in Fig. 2c–d. From Fig. 2c, it can be observed that the Co-doped material exhibits a spherical structure, which stacks into a rod-like structure with small sizes and is accompanied by agglomeration. The high-magnification image shows that the surface of the Co-V_2O_5 material becomes rough. This rough surface structure enables V_2O_5 to expose more active sites and a larger specific surface area, which is beneficial for proton transfer in the electrolyte and hydrogen evolution. Fig. 2e–f show HRTEM images of V_2O_5 and cobalt-doped V_2O_5 samples, respectively. From the HRTEM image of the V_2O_5 sample in Fig. 2e, the interplanar spacing is measured to be 0.336 nm, which can be indexed to the (110) crystal plane. The Co-doped V_2O_5 sample has a larger lattice spacing of 0.341 nm, which is larger than that of pure V_2O_5. This indicates that Co has been doped into the V_2O_5 lattice. Fig. 2g further confirms the presence of various elements. From the figure, it can be observed that elements such as Co, V, and O are uniformly distributed on the Co-V_2O_5 nanospheres, thus confirming the presence of Co.

3.2 Hydrogen evolution performance of samples in alkaline solution

To investigate the electrocatalytic performance of these materials under different pH conditions, a series of hydrogen evolution reaction and oxygen evolution reaction experiments were conducted using a three-electrode system. Fig. 3 shows the HER performance of the samples in different electrolytes, and Fig. 3a–c present the electrochemical performance measured in 1 M KOH solution. As shown in Fig. 3a, the linear sweep voltammetry (LSV) curves of the four prepared materials, nickel foam, and noble metals are compared. It was found that at a current density of 10 mA cm^{-2}, the Co-V_2O_5-6% sample exhibited an overpotential of only 104 mV. As shown in Table 1, the pristine V_2O_5 exhibits a relatively high overpotential of 168 mV at 10 mA cm^{-2}, which is a common limitation of pure vanadium oxide catalysts in alkaline HER. By introducing Co doping, the overpotential of V_2O_5 is significantly reduced: the Co-V_2O_5-6% catalyst achieves an overpotential of 104 mV, outperforming representative non-noble metal catalysts such as

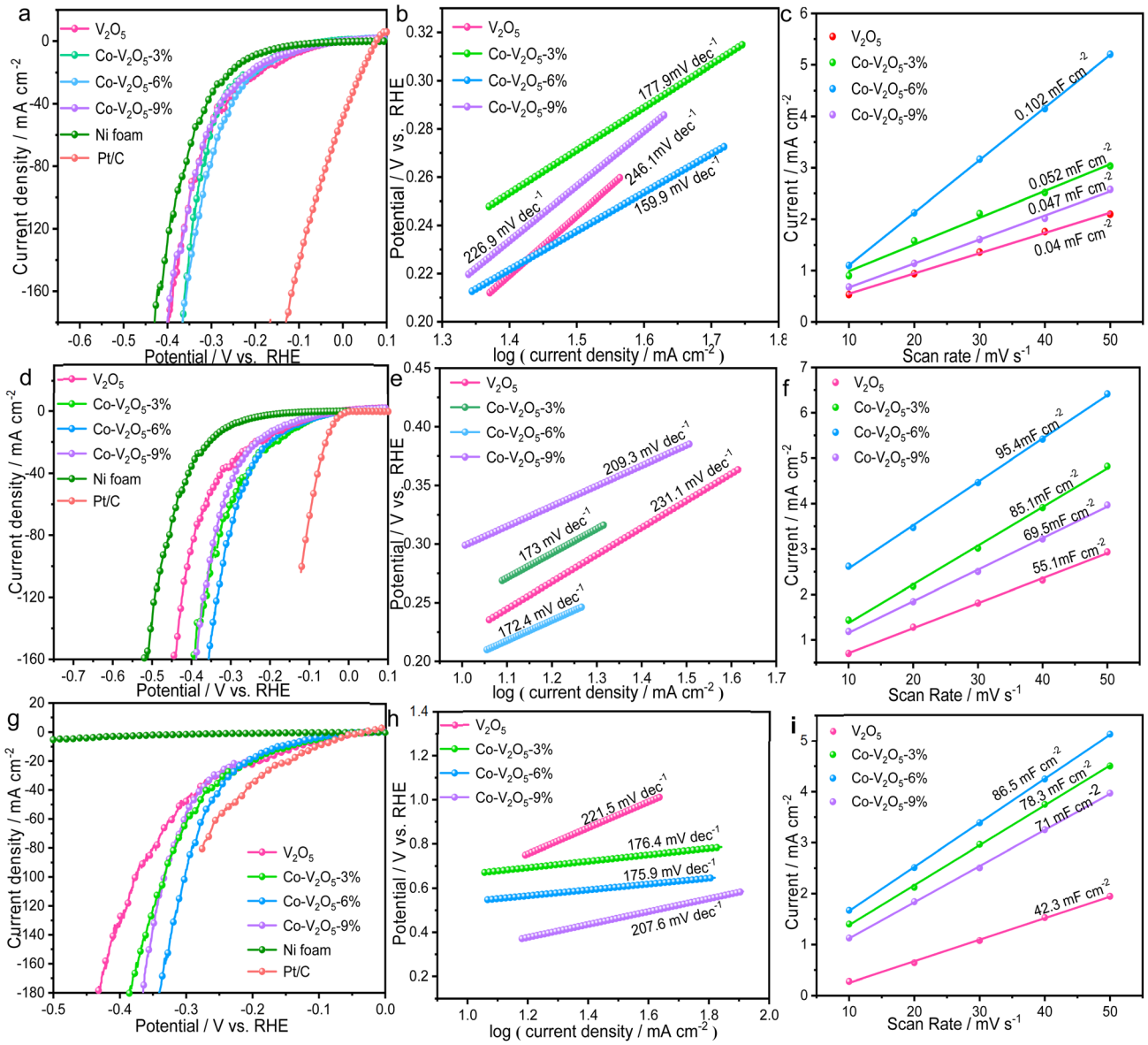

Fig. 3 HER performances of the electrocatalysts (a) LSV curves in 1.0 M KOH (b) Tafel plots (c) double-layer capacitance (d) LSV curves in acidic solution (e) Tafel plots (f) double-layer capacitance (g) LSV curves in 1.0 M PBS (h) Tafel plots (i) double-layer capacitance.

Table 1 HER electrocatalytic performance of several electrode materials

Materials	Overpotential (mV)	Electrolyte	Ref.
V_2O_5	168 (10 mA cm^{-2})	1.0 M KOH	This work
Co-V_2O_5-3%	125(10 mA cm^{-2})	1.0 M KOH	This work
Co-V_2O_5-6%	104 (10 mA cm^{-2})	1.0 M KOH	This work
Co-V_2O_5-9%	156 (10 mA cm^{-2})	1.0 M KOH	This work
Co/VN/NC-8	116 (10 mA cm^{-2})	1.0 M KOH	36
Co_2CuO_4	127 (10 mA cm^{-2})	1.0 M KOH	37
CuCoS	158 (10 mA cm^{-2})	1.0 M KOH	38
Co–$NiSe_2$/NF	136 (10 mA cm^{-2})	1.0 M KOH	39
$Co_9S_8Cu_2S$	134 (10 mA cm^{-2})	1.0 M KOH	40

Co/VN/NC-8 (116 mV), Co_2CuO_4 (127 mV), and Co–$NiSe_2$/NF (136 mV) under the same test conditions. This comparison clarifies the research motivation: pure V_2O_5 suffers from high HER overpotential in alkaline media, while existing non-noble metal catalysts still have room for activity optimization. Our research objective is to regulate the electronic structure of V_2O_5 *via* transition metal (Co) doping, thereby improving its HER performance and providing a feasible strategy for developing efficient vanadium-based non-noble metal electrocatalysts. This indicates that Co doping improved the HER performance. The overpotentials of other samples were as follows: V_2O_5 (168 mV), Co-V_2O_5-3% (125 mV), and Co-V_2O_5-9% catalyst (156 mV). Subsequently, the measured polarization curves were linearly fitted to analyze the Tafel slopes of these samples, thereby exploring the reaction kinetics mechanism of HER in more detail. As observed in Fig. 3b, the Tafel slope of the Co-V_2O_5-6% electrode (159.9 mV dec^{-1}) was much smaller than those of V_2O_5 (246.1 mV dec^{-1}), Co-V_2O_5-3% (177.9 mV dec^{-1}), and Co-V_2O_5-9% (226.9 mV dec^{-1}). A smaller Tafel slope indicates that

the HER reaction of the Co-V_2O_5-6% electrode follows the Volmer–Heyrovsky mechanism and exhibits faster HER reaction kinetics compared to other materials.

In alkaline solutions, the HER process consists of three steps: (i) volmer reaction (120 mV dec^{-1}), (ii) Heyrovsky reaction (40 mV dec^{-1}), and (iii) Tafel reaction (30 mV dec^{-1}).[28,29] Based on the Tafel slope of the Co-V_2O_5-6% material, the electrode undergoes HER *via* the Volmer–Heyrovsky mechanism, where the electrochemical desorption step determines the reaction rate.[30–32] Investigate ECSA through C_{dl} to further explore the mechanism and kinetics of electrocatalytic reactions.[33] As observed in Fig. 4c, the C_{dl} values of the prepared V_2O_5, Co-V_2O_5-3%, Co-V_2O_5-6%, and Co-V_2O_5-9% samples were 0.04 mF cm^{-2}, 0.052 mF cm^{-2}, 0.102 mF cm^{-2}, and 0.047 mF cm^{-2}, respectively. The C_{dl} value of the Co-V_2O_5-6% sample was much larger than those of the other samples, confirming its optimal performance. A larger C_{dl} value indicates a larger specific surface area of HER active sites and a higher density of active sites. In conclusion, appropriate Co doping modifies the morphology of the original material, which in turn changes the size of the electrochemical active surface area and ultimately enhances the electrocatalytic performance of the material. Electrochemical impedance spectroscopy (EIS) measurements were performed in alkaline electrolyte to investigate electron and ion transport. Fig. S1a presents the Nyquist plots of the prepared materials. The high-frequency region of the curve represents the charge transfer resistance, while the low-frequency straight line represents the ion diffusion resistance. Compared with other doping concentrations and pure V_2O_5, the Co-V_2O_5-3% material exhibited the highest slope of the low-frequency straight line, indicating the smallest ion diffusion resistance, faster ion transport rate, and better electronic conductivity.

The ion diffusion rate can also be analyzed using eqn:

$$Z = R_s + R_{ct} + \sigma_w \omega^{-1/2}$$

where σ_w is the Warburg factor, ω is the angular frequency, and Z is the diffusion resistance of OH^-.

Stability is one of the key indicators for evaluating catalyst performance. Therefore, Fig. S1b shows the long-term HER cycling stability tests of the Co-V_2O_5-3%, V_2O_5, Co-V_2O_5-6%, and Co-V_2O_5-9% electrode materials. The tests revealed that the Co-V_2O_5-3% material exhibited excellent cycling stability. Furthermore, the Co-V_2O_5-3% catalyst maintained excellent stability at a current density of 10 mA cm^{-2} for 12 hours. The other samples showed no significant changes within 12 hours at current densities of 9, 12, and 13 mA cm^{-2}, respectively. These results confirm that the prepared Co-V_2O_5 materials exhibit excellent stability in an alkaline environment.

3.3 Hydrogen evolution performance of samples in acidic solution

Subsequently, the HER activity of different materials under acidic conditions was tested. Fig. 3d shows the polarization curves of different materials in 0.5 M H_2SO_4 solution. At a current density of 10 mA cm^{-2}, the overpotential of the Co-V_2O_5-6% material (127 mV) was lower than that of V_2O_5 (190 mV), Co-V_2O_5-3% (147 mV), and Co-V_2O_5-9% (173 mV). After the introduction of Co ions, the HER activity of V_2O_5 materials with

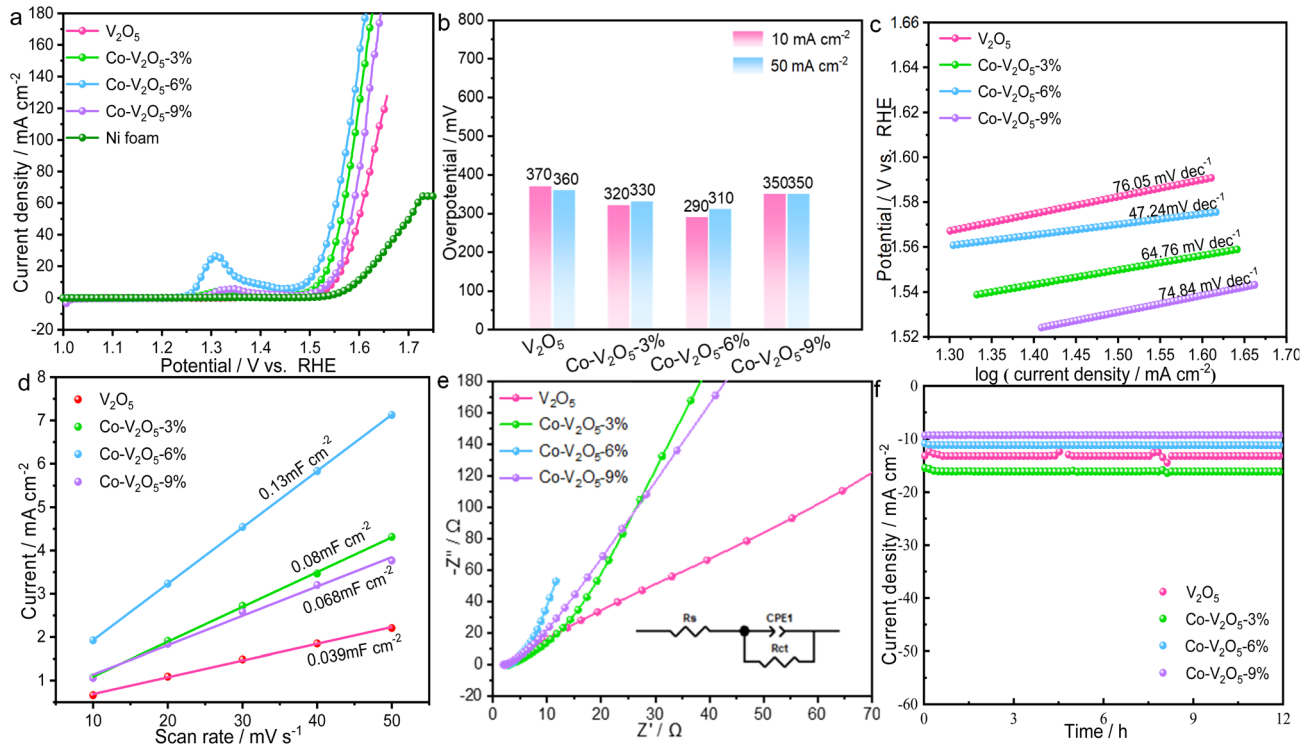

Fig. 4 OER performances of the as-prepared samples (a) LSV curves in 1.0 M KOH solution (b) overpotentials of the material at current densities of 10 mA cm^{-2} and 50 mA cm^{-2} (c) Tafel plots (d) CV curves of double-layer capacitance (e) Nyquist curves (f) chronoamperometric stability tests.

different Co contents was improved. Through comprehensive analysis, it was concluded that the Co-V_2O_5-6% material exhibited higher electrocatalytic activity than the Co-V_2O_5-9% and Co-V_2O_5-3% samples. This may be attributed to the excessive Co ions depositing on the catalyst surface, thereby covering some of the active sites.

In addition, in-depth research was conducted on the Tafel plots to explore the HER kinetic characteristics of these materials. As shown in Fig. 3e, the Tafel slope of the Co-V_2O_5-6% material (172.4 mV dec^{-1}) was smaller than that of V_2O_5 (190 mV dec^{-1}) and the remaining Co-doped V_2O_5 materials. This indicates that the doped substance can significantly enhance the catalytic efficiency of the samples and improve HER kinetics.[34,35] The Co-V_2O_5-6% material exhibited a lower Tafel slope, implying that the HER process follows the Volmer–Heyrovsky mechanism:

$$H^+ + e^- + Cat. \rightarrow H_{ads}(Volmer\ step)$$

$$H^+ + e^- + H_{ads} \rightarrow H_2\ (Heyrovsky\ step)$$

Subsequently, electrochemical impedance spectroscopy (EIS) technology was used to conduct an in-depth study on the impedance characteristics of the electrode materials. As shown in Fig. S1d, the Co-V_2O_5-6% material had the highest slope of the low-frequency straight line and the smallest ion diffusion resistance, which means it has a faster ion transport rate and excellent electronic conductivity. The results show that the Co-V_2O_5-6% product has a faster electron transfer rate at the interface between the electrolyte and the electrocatalyst and exhibits the optimal HER kinetics. Experimental results demonstrate that the Co-V_2O_5-6% product shows a high electron transfer rate and excellent HER kinetic performance at the interface between the electrolyte and the electrocatalyst.

3.4 Hydrogen evolution performance of samples in neutral solution

Finally, the HER performance of the target material in a neutral electrolyte (1.0 M PBS solution). As shown in Fig. 3g, under the neutral electrolyte environment, the Co-V_2O_5-6% material exhibited a lower overpotential (167 mV) and higher catalytic activity than the other comparative materials (V_2O_5: 220 mV, Co-V_2O_5-3%: 175 mV, Co-V_2O_5-9%: 207 mV). Experimental results confirm that either excessive or insufficient doping content does not significantly enhance the HER activity of the material. As observed in Fig. 3h, the Tafel slope of the Co-V_2O_5-6% material (175.9 mV dec^{-1}) was significantly lower than that of V_2O_5 (221.5 mV dec^{-1}), Co-V_2O_5-3% (176.4 mV dec^{-1}), and Co-V_2O_5-9% catalyst (207.6 mV dec^{-1}). This indicates that the Co-V_2O_5-6% material has the fastest reaction rate during the HER process. According to Fig. S1e, electrochemical impedance spectroscopy (EIS) was used to analyze the reaction kinetics of all studied materials. The results show that the Co-V_2O_5-6% material exhibited a higher slope in the high-frequency region than other materials, indicating it has the smallest ion transfer resistance. Compared with the other three materials, the Co-V_2O_5-6% material demonstrated excellent charge transfer capability and HER kinetics. The HER mechanism in neutral electrolytes is generally consistent with that in acidic and alkaline electrolytes. However, in neutral conditions, the low proton concentration increases electron transfer resistance, leading to a higher overpotential. Therefore, the Co-V_2O_5-6% material exhibited a lower overpotential in alkaline conditions than in the other two electrolytes, suggesting an accelerated HER reaction rate in the alkaline environment. It can thus be concluded that Co-V_2O_5-6% more effectively promotes the electrochemical reaction of hydrogen ions in alkaline electrolytes.

3.5 Oxygen evolution performance of samples in alkaline solution

Subsequently, the OER performance of the samples under the same alkaline environment was studied, with specific results shown in Fig. 4 below. Fig. 4a depicts the LSV curves of different samples. It can be observed that when the current density reached 10 mA cm^{-2}, the overpotential of the Co-V_2O_5-6% material was 290 mV, while those of V_2O_5, Co-V_2O_5-3%, and Co-V_2O_5-9% were 370 mV, 320 mV, and 350 mV, respectively. Compared with these materials, Co-V_2O_5-6% had the lowest overpotential, indicating its OER activity is much higher than that of other materials. Appropriate Co doping significantly improved OER activity. By comparing the overpotentials of different materials, it was observed that the catalytic performance of V_2O_5 was much lower than that of other materials. With the introduction of Co, the performance of Co-V_2O_5 materials gradually improved: Co-V_2O_5-3% showed enhanced performance, Co-V_2O_5-6% exhibited the optimal performance, and Co-V_2O_5-9% showed a decline when the Co content continued to increase. Subsequently, the Tafel slope method was used to explore the electron transfer kinetics on the catalyst surface during the OER process. As shown in Fig. 4c, the Tafel slope of the Co-V_2O_5-6% material was 47.24 mV dec^{-1}, while that of V_2O_5 was 76.05 mV dec^{-1} (much higher than Co-V_2O_5-6%). Co doping modified the morphology of the original V_2O_5 material, significantly improving electron and ion transfer for OER and increasing active sites. The Co-V_2O_5-6% material had the lowest Tafel slope among the doped samples; the Tafel slopes of other materials were 64.76 mV dec^{-1} (Co-V_2O_5-3%) and 74.84 mV dec^{-1} (Co-V_2O_5-9%), indicating that 6% Co content enhances reaction kinetics. Fig. 4d shows the electrochemical double-layer capacitance (C_{dl}) values of the synthesized materials. It can be observed that the C_{dl} value of the Co-V_2O_5-6% material (0.13 mF cm^{-2}) was much higher than that of the other samples (V_2O_5: 0.039 mF cm^{-2}, Co-V_2O_5-3%: 0.08 mF cm^{-2}, Co-V_2O_5-9%: 0.068 mF cm^{-2}). Accordingly, Co-V_2O_5-6% exhibited the optimal electrocatalytic performance. Fig. 4e presents the impedance spectra of the studied materials. It can be seen that the Co-V_2O_5-6% material had the largest linear slope compared with other doped materials and pure V_2O_5. Since the linear slope represents the rate of ion diffusion, the Co-V_2O_5-6% material had the fastest diffusion rate and the smallest resistance, which to a certain extent reduced the OER overpotential of the material. Based on the fitted data, Co-V_2O_5-6% exhibits superior charge transfer efficiency over other

samples. To ensure physical consistency and reliable material comparison, the electrochemical impedance spectroscopy data were analyzed using the equivalent circuit shown below, which comprises a solution resistance (R_s) in series with a parallel combination of a constant phase element (CPE, representing the non-ideal double-layer capacitance) and the charge transfer resistance (R_{ct}).

The fitted R_s values are 3.162, 2.651, 2.403, and 2.973 Ω, and the fitted R_{ct} values are 79.502, 72.735, 53.931, and 62.401 Ω (see Table S1). In particular, Co-V_2O_5-6% displays the lowest R_{ct} value, indicating the smallest charge transfer barrier and the fastest interfacial electron transfer kinetics for this optimal sample. Furthermore, the CPE parameters elucidate the structural characteristics of the electrode surface. Co-V_2O_5-6% achieves the highest CPE-P value among all samples, signifying the most ideal capacitive behavior and the most uniform electrode–electrolyte interface. Consistently, Co-V_2O_5-6% shows the narrowest semicircle in the high-frequency region. (page 14 of the revised manuscript).

3.6 Performance of the assembled overall water splitting system

Next, an overall water splitting system was assembled to investigate the performance of the synthesized materials as bifunctional catalysts for water electrolysis. Through a series of experiments, the measured experimental data are shown in the figures below. As observed in Fig. 5a, a simple two-electrode water electrolysis system was constructed using the prepared materials as electrodes and electrolytic cell devices. During the reaction, H_2 evolution was observed at the cathode and O_2 evolution at the anode, with a large number of bubbles appearing on the surface of the materials (as shown in the figure below). By observing the LSV curves of all materials in Fig. 5b, it was found that at a current density of 10 mA cm^{-2}, the cell voltages of V_2O_5, Co-V_2O_5-3%, Co-V_2O_5-6%, and Co-V_2O_5-9% materials were 1.65 V, 1.5 V, 1.38 V, and 1.63 V, respectively. It can be seen that the Co-V_2O_5-6% material had the lowest overpotential compared with the other materials, thus exhibiting the most excellent electrocatalytic performance. In addition, by studying the impedance spectra of the prepared materials (Fig. S1f), it can be observed that the Co-V_2O_5-6% material had the largest linear slope in the low-frequency region. A larger slope indicates a higher ion diffusion rate and smaller ion diffusion resistance, which in turn means the Co-V_2O_5-6% material has a faster electron and ion conduction rate. Finally, the cycling stability of the materials was investigated (Fig. 5c). A long-term overall water splitting stability test of the samples in the electrolyte showed that the Co-V_2O_5-6% material maintained a stable potential after 12 hours without significant fluctuations, indicating excellent long-term stability.

3.7 Structural characterization of catalyzed materials

Fig. S2a and b show morphological features were examined by SEM and TEM images of the post-catalyzed Co-V_2O_5, which

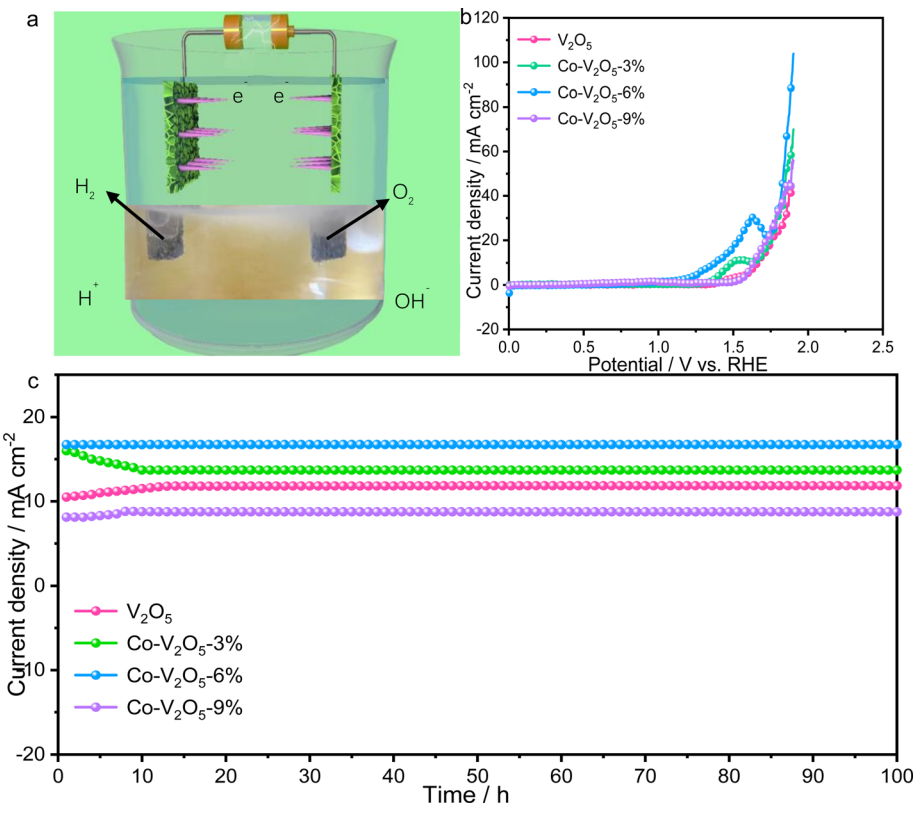

Fig. 5 Overall water splitting performance of the samples (a) schematic diagram of the overall water splitting device (b) LSV curves (c) constant voltage cycling plot.

revealed that the catalyst largely retained its original nanospheres without obvious collapse or aggregation, indicating excellent structural robustness. As shown in Fig. S3a, compared with the pristine state before water electrolysis, the characteristic peaks of O 1s, V 2p, Co 2p, and C 1s in the XPS survey spectrum of the Co-V_2O_5 catalyst show no obvious shifts, and the chemical state composition of each element remains stable. Although the intensities of some peaks decrease slightly, all characteristic peaks are clearly distinguishable, indicating that the surface elemental composition and chemical environment of the catalyst do not undergo essential changes after long-term electrolysis. Based on the XPS analysis is shown in Fig. S3(b–d), the Co-V_2O_5 catalyst undergoes reversible valence state reconstruction ($V^{5+} \rightarrow V^{4+}$ and $Co^{3+} \rightarrow Co^{2+}$) during water electrolysis, which enhances its electrocatalytic activity while maintaining excellent structural stability.

As shown in Fig. S5(a and b), selected area electron diffraction measurements of the material before and after electrocatalysis show diffraction rings corresponding to crystal planes of V_2O_5, which is consistent with the XRD results. Materials prior to electrocatalysis, the SAED pattern exhibits a clear, well-defined and continuous polycrystalline diffraction ring with clear boundaries and regular spot distribution. After electrocatalysis, the SAED pattern shows a slightly broadened but still pronounced polycrystalline diffraction ring with no apparent amorphization or new impurity phase signal. This indicates that the electrocatalyst maintains a good polycrystalline crystallinity after catalysis, and the crystallinity decreases only slightly due to electrochemical cycling, reflecting its excellent structural stability under catalytic conditions.

4. Conclusion

In summary, we successfully prepared cobalt (Co)-doped V_2O_5 materials *via* a simple hydrothermal synthesis method. The Co-doped materials exhibited a spherical structure, which can expose more active sites and a larger specific surface area—both beneficial for proton transfer in the electrolyte and hydrogen evolution. The Co-V_2O_5-6% material showed excellent HER and OER performance in 0.5 M H_2SO_4, 1.0 M PBS, and 1.0 M KOH solutions, with advantages such as low overpotential, low Tafel slope, large capacitance, and long-term cycling stability. In addition, it exhibited excellent electrocatalytic performance for efficient water splitting, with a cell voltage of 1.38 V and long durability.

Conflicts of interest

The authors declare no conflict of interest.

Data availability

The author declare that there is no data to share.

Supplementary information (SI): electrochemical performance and structural characterization data. See DOI: https://doi.org/10.1039/d6ra00151c.

References

1 Y. Chen, *et al.*, A catalytic cycle that enables crude hydrogen separation, storage and transportation, *Nat. Energy*, 2025, **10**(8), 971–980.
2 L. wang, *et al.*, Rational d-Orbitals Modulation for Tailoring Co2P Interfacial Adsorption Behavior: Boosting Alkaline Hydrogen Evolution, *Adv. Energy Mater.*, 2025, e04036.
3 H. Zhou, *et al.*, In situ reconstructed amorphous MOOH enhanced NiCoP@NiFe-LDH bifunctional electrocatalyst for long durable seawater electrolysis, *Inorg. Chem. Front.*, 2026, **13**, 666–679.
4 S. Xu, *et al.*, Challenges and Emerging Trends in Hydrogen Energy Industrialization: From Hydrogen Evolution Reaction to Storage, Transportation, and Utilization, *Small*, 2025, **21**(24), 2502000.
5 T. Hisatomi, *et al.*, Materials and systems for large-scale photocatalytic water splitting, *Nat. Rev. Mater.*, 2025, **10**(10), 769–782.
6 G. Centi and S. Perathoner, Electrocatalysis: Prospects and Role to Enable an E-Chemistry Future, *Chem. Rec.*, 2025, **25**(6), e202400259.
7 Y. Liu, *et al.*, Corrosion-Driven Ni3S4 Gradient in NiFe-LDH Enables Durable Industrial-Scale Water Electrolysis, *Angew. Chem., Int. Ed.*, 2025, e202516894.
8 G. Xu, *et al.*, Constructing Ultra-Stable Electrocatalysts to Achieve Adaptability of Industrial-Level Alkaline Water Electrolyzers for Fluctuating Renewable Energies, *Adv. Energy Mater.*, 2025, **15**(31), 2500926.
9 F. Lyu, *et al.*, Noble-Metal-Free Electrocatalysts for Oxygen Evolution, *Small*, 2018, **15**(1), 1804201.
10 K. Zeng, *et al.*, Surface-Decorated High-Entropy Alloy Catalysts with Significantly Boosted Activity and Stability, *Adv. Funct. Mater.*, 2022, **32**(33), 2204643.
11 H. Liang, *et al.*, Operando Mobile Catalysis for Reverse Water Gas Shift Reaction, *Angew. Chem., Int. Ed.*, 2024, **63**(12), e202318747.
12 C. Jia, *et al.*, Challenges and Opportunities for Single-Atom Electrocatalysts: From Lab-Scale Research to Potential Industry-Level Applications, *Adv. Mater.*, 2024, **36**(42), 2404659.
13 H. Zhou, *et al.*, Interface-Engineered NiSe/Ni-Fe-P Nanocubes for Efficient and Durable Seawater Electrolysis, *ACS Appl. Mater. Interfaces*, 2025, **17**(47), 64340–64353.
14 H. Liu, *et al.*, Distorting Local Structures to Modulate Ligand Fields in Vanadium Oxide for High-Performance Aqueous Zinc-Ion Batteries, *ACS Nano*, 2025, **19**(9), 9132–9143.
15 A. Guo, *et al.*, A Comprehensive Review of the Mechanism and Modification Strategies of V2O5 Cathodes for Aqueous Zinc-Ion Batteries, *ACS Nano*, 2024, **18**(40), 27261–27286.
16 G. Li, Z. Yao and C. Li, In-situ multi-scale structural engineering of cathode and electrolyte for high-rate and long-life Mg metal batteries, *J. Energy Chem.*, 2025, **105**, 44–53.
17 Q. Wei, *et al.*, Pseudocapacitive layered iron vanadate nanosheets cathode for ultrahigh-rate lithium ion storage, *Nano Energy*, 2018, **47**, 294–300.

18 Y. Wanga, S. Weia, Z.-H. Qia,S. Chena, K. Zhua, H. Dinga, Y. Caoa, Q. Zhoua, C. Wanga, P. Zhanga, X. Guoa, X. Yanga, X. Wub and Li Song, *Intercalant-induced V T2g Orbital Occupation in Vanadium Oxide Cathode toward Fast-Charging Aqueous Zinc-Ion Batteries*, Proceedings of the National Academy of Sciences, 2022.

19 A. Wang, *et al.*, Building stabilized Cu0.17Mn0.03V2O5−□·2.16H2O cathode enables an outstanding room-/low-temperature aqueous Zn-ion batteries, *Carbon Energy*, 2024, **6**(8), e512.

20 Y. Dai, *et al.*, S-doped VO2 induced oxygen vacancies for achieving high performance aqueous zinc ion batteries, *Chem. Eng. J.*, 2025, 523.

21 B. Nie, *et al.*, Pre-Zincification of Sandwiched V2O5 to Accelerate Intercalation Kinetics and Mitigate Cathodic Passivation in Low N/P Ratio Zinc-Ion Pouch Cells, *Nano Lett.*, 2025, **25**(27), 10935–10943.

22 X. Zhao, *et al.*, 3d-Orbital Regulation of Transition Metal Intercalated Vanadate as Optimized Cathodes for Calcium-Ion Batteries, *Adv. Funct. Mater.*, 2023, **34**(2), 2309753.

23 Q. Zong, *et al.*, Dual Effects of Metal and Organic Ions Co-Intercalation Boosting the Kinetics and Stability of Hydrated Vanadate Cathodes for Aqueous Zinc-Ion Batteries, *Adv. Energy Mater.*, 2023, **13**(31), 2301480.

24 F.-J. Liu, *et al.*, Cation-doped V2O5 microsphere as a bidirectional catalyst to activate sulfur redox reactions for lithium-sulfur batteries, *Chem. Eng. J.*, 2023, **456**, 140948.

25 Q. Li, *et al.*, Co doped V2O5 hollow microsphere as high-performance cathode for aqueous zinc-ion battery, *J. Power Sources*, 2025, **628**, 235895.

26 Z. Li, *et al.*, Enabling giant thermopower by heterostructure engineering of hydrated vanadium pentoxide for zinc ion thermal charging cells, *Nat. Commun.*, 2023, **14**(1), 6816.

27 Q. Li, *et al.*, Triple Redox–Enabled High-Entropy Metal–Organic Coordination Driving High-Performance Aqueous Zinc–Ion Batteries, *Advanced Science*, 2025, e11748.

28 P.-C. Tsai, *et al.*, Single-particle measurements of electrochemical kinetics in NMC and NCA cathodes for Li-ion batteries, *Energy Environ. Sci.*, 2018, **11**(4), 860–871.

29 L. B. T. de Kam, T. L. Maier and K. Krischer, Electrolyte effects on the alkaline hydrogen evolution reaction: A mean-field approach, *Electrochim. Acta*, 2024, **497**, 144530.

30 Y. Yang, *et al.*, CoNiSe2 heteronanorods decorated with layered-double-hydroxides for efficient hydrogen evolution, *Appl. Catal., B*, 2019, **242**, 132–139.

31 M. Li, *et al.*, A Fractal-Tip Cu3Ni/NiMoO4 Heterostructure for Efficient Hydrogen Evolution via an Accelerated Volmer–Tafel Mechanism, *ACS Nano*, 2025, **19**(40), 35647–35657.

32 S. M. Parsa, *et al.*, 15 Years of Progress on Transition Metal-Based Electrocatalysts for Microbial Electrochemical Hydrogen Production: From Nanoscale Design to Macroscale Application, *Nano-Micro Lett.*, 2025, **17**(1), 303.

33 A. Muthurasu, V. Maruthapandian and H. Y. Kim, Metal-organic framework derived Co3O4/MoS2 heterostructure for efficient bifunctional electrocatalysts for oxygen evolution reaction and hydrogen evolution reaction, *Appl. Catal., B*, 2019, **248**, 202–210.

34 Y. Lee, *et al.*, Graphene-based stretchable/wearable self-powered touch sensor, *Nano Energy*, 2019, **62**, 259–267.

35 H. Zheng, *et al.*, H2 Evolution with Silicotungstic Acid Electron Mediator over V-Doped MoS2 Electrocatalysts, *ACS Energy Lett.*, 2025, **10**(2), 678–684.

36 X. Li, *et al.*, Cobalt/Vanadium Nitride Nano-Heterojunction Supported on N-Doped Nanocarbon for Alkaline Overall Water Splitting, *ACS Appl. Nano Mater.*, 2025, **8**(14), 7026–7038.

37 S. Sekar, *et al.*, Unlocking the Cu-Co Interplay: Electrodeposited Spinel Co2CuO4 as a High-Performance Hydrogen Evolution Catalyst, *Int. J. Mol. Sci.*, 2025, **26**(22), 11226.

38 K. K. Joshi, *et al.*, Efficient hybrid water splitting and direct electrooxidation of organic dye from wastewater using copper cobalt sulphide nanosheets, *Int. J. Hydrogen Energy*, 2024, **58**, 1562–1575.

39 G. Li, *et al.*, Co-NiSe2/NF nanosheet for efficient hydrogen evolution reaction, *Catal. Commun.*, 2022, **165**, 106443.

40 F. Qiao and X. Xu, Nanostructured Cobalt and Copper Sulfides for Applications as Electrocatalysts for High-Efficiency Alkaline Hydrogen Evolution, *ACS Appl. Nano Mater.*, 2025, **8**(28), 14420–14427.